Coherent Networks of Plasmonic Dipole Domains: Long-Range Optical Coupling of Phase-Correlated Packages of Metallic Nanoparticles

Seyed M. Sadeghi[1,*] and Rithvik R. Gutha[2]

[1] *Department of Physics and Astronomy, University of Alabama in Huntsville, Huntsville, Alabama 35899, USA*
[2] *Department of Physics and Astronomy, Living Systems Institute, University of Exeter, Exeter EX4 4QD, United Kingdom*

(Received 1 December 2020; revised 11 January 2021; accepted 10 February 2021; published 5 March 2021)

Through the use of experimental and numerical techniques, we study coherent networks of plasmonic phase-correlated dipole domains that can spread coherent properties along ultralong distances. The phase-correlated domains occur in regions containing closely packed metallic nanoparticles with random positions, shapes, and sizes. We demonstrate that when such regions are periodically arranged, forming two-dimensional arrays, optical diffraction can coherently excite and align the plasmonic dipoles of the nanoparticles within each region, forming delocalized collective plasmon resonances associated with the in-phase coupling of the dipoles. We study the impact of the number of metallic nanoparticles in each region, determining the limit at which it becomes a phase-correlated dipole domain and establishes coherent interdomain coupling. Our results show how such a coupling can form coherent networks of packages of delocalized states with the same phase information. Au nanoislands with different packings, sizes, and shapes are considered as experimental models to explore phase-correlated dipole domains and interdomain coupling. The conditions in which the coherent interdomain coupling occurs via parallel or orthogonal hybridization of the Rayleigh anomaly with the delocalized plasmon resonances supported by the domains are explored. The outcomes offer alternative techniques for coherent transport of energy and information, in which phase-correlated dipole domains serve as units with large coherent spatial extension.

DOI: 10.1103/PhysRevApplied.15.034018

I. INTRODUCTION

The transport of electromagnetic energy via localized surface-plasmon resonances (LSPRs) in chains of closely packed metallic nanoparticles (MNPs) has been studied extensively [1–5]. Such a process occurs below the diffraction limit and can convert the optical mode into nonradiating surface plasmons, enhancing the energy-transport range [6,7]. A prime advantage of such structures is their ability to transport energy around the corners, offering flexible interconnects [4,8]. Chains of MNPs can also be used for sensing applications, taking advantage of the plasmonic shift associated with the variations of the spacing between the MNPs [9]. Moreover, recent reports have investigated the near field associated with transverse plasmonic wave propagation in a chain of elliptical gold nanocylinders fed by a silicon refractive waveguide at optical telecommunication wavelengths [10]. The reports also include study of radiation and retardation effects in one-dimensional plasmonic systems with nontrivial topologies [11]. These investigations expand the horizon for propagation of pulse-like energy propagation through one-dimensional arrays of dipoles with branches and gates [12].

In a recent report, we experimentally investigated the optics of periodic arrays of regions that contained densely packed Au nanoislands (NISs) with a random distribution of sizes and positions [13]. We demonstrated the conditions in which such arrays can support a unique form of surface lattice resonances (SLRs). Such resonances are formed via hybridization of the LSPRs of the NISs with the diffraction modes of the arrays at certain frequencies [14–16]. The presence of such resonances offers the conditions in which the plasmonic dipoles of the NISs are coherently excited and coupled to the diffractive modes of the lattice or Rayleigh anomaly (RA). SLRs are known to have applications ranging from biological and chemical sensing [17–25] to excitonic laser systems [26–28], optical filters [29], control of the emission of quantum emitters [26,28], perfect absorbers [30], and quantum information [31].

By means of experimental measurements and simulation, we study the formation of phase-correlated dipole domains (PCDDs) in periodic arrays of unit regions (URs) containing different random distributions of Au NISs

*seyed.sadeghi@uah.edu

(Fig. 1). PCDDs happen when the NISs are coupled to each other, in phase, via the stimulated plasmonic dipoles that are coherently excited and aligned by the optical diffraction modes of the arrays. Under these conditions, each UR [Figs. 1(b)–1(e)] accommodates coherent near-field coupling between NISs at frequencies that are quite different from those of the LSPRs of the NISs, supporting unique collective resonances. The PCDDs studied in this paper offer unique photonic-plasmonic scenarios in which the coherent nature of the lattice modes of the arrays is used to significantly enhance inter-NIS coupling. We study the impact the number of nanoparticles per each UR, determining the limit that allows PCDDs and their optical coupling with the neighboring domains to happen. The results demonstrate the conditions in which the interdomain coupling occurs efficiently via their diffractive coupling to RAs, offering a coherent network of PCDDs. URs with different plasmonic architectures [Fig. 1(b)–1(e)] are considered as experimental models to explore PCDDs and their coherent coupling. These architectures determine the conditions in which the interdomain coupling occurs via parallel or orthogonal hybridization with the RA. We explore how the near-field coupling within each UR plays a key role in the formation of PCDDs and the long coherent networks of these domains.

The outcomes of this paper may offer alternative techniques for ultrafast coherent transport of energy and information. In particular, knowledge of the optimal plasmonic architectures for URs that can lead to efficient interdomain coupling will be particularly useful for investigation of the transport processes, in which instead of individual nanoparticles, one considers PCDDs [32]. Additionally, the prospect of coherent coupling of a large ensemble of plasmonic dipoles can set up a unique horizon for plasmonic-photonic processes and applications. These include enhanced optical absorption and cross sections of dipoles [31] and two-dimensional atomic lattices [33].

II. EXPERIMENTAL AND SIMULATION METHODOLOGIES

For the experimental part, *e*-beam lithography using a Zeiss LEO 1550 scanning electron microscope (SEM) is utilized to fabricate four types of samples (samples 1–4). This technique is used to construct a template (lattice), as shown in Fig. 1(a). This template contains a layer of resist on glass, with open regions with nominal lateral dimensions of $L \sim 800$ and $W \sim 200$ nm. These regions serve as URs. The lattice constants of the template along the x axis and y axis, a_x and a_y, are also considered to be 1000 and 500 nm, respectively [Fig. 1(a)]. After this, we use a thermal evaporator (CVC Vacuum Evaporation System) to deposit thin layers of Au with a mass thicknesses between 5 and 10 nm on the top. The structures are then placed in a lift-off solution for about 10 h and washed thoroughly. This is followed by thermal annealing at 500 C for 30 min. The plasmonic architectures of the URs of samples 1–4 are shown in Figs. 1(b)–1(e), respectively. In the case of sample 1, the NISs are small and closely packed [Fig. 1(b)]. In the case of sample 2, the NISs are relatively larger but their numbers per UR are much less [Fig. 1(c)]. In the case of sample 3, the URs contain larger NISs that are connected to each other [Fig. 1(d)]. Figure 1(e) shows a plasmonic architecture that lacks discrete NISs. A transmission setup equipped with a sensitive spectrometer (Ocean Optics TE-cooled QE-pro) is used to measure the extinction spectra of these samples. This is done when the superstrate is air (n_{sup}=1) or methanol ($n_{sup} \sim 1.33$). The incident light is considered to be polarized along either the x axis (x-pol) or y axis (y-pol) of the URs [Fig. 1(a)].

To investigate the concept of the PCDD and coherent inter-PCDD coupling numerically, we use the finite-difference time-domain (FDTD) method to explore the optical mode properties of periodic arrays of URs [Fig. 1(a)] with plasmonic architectures similar to those shown in Figs. 1(b)–1(e). For this, we consider that the URs are represented by regions of length L, width W, and height H. Similar to the experimental part [Fig. 1(a)], these regions are periodically arranged, forming a two-dimensional lattice with $a_x = 1$ μm and $a_y = 0.5$ μm. Each region is considered to contain a given number of Au nanospheres (N) with random locations. The range of radii of such nanospheres (r) is chosen such that they form URs with overall features similar to those considered in Figs. 1(b)–1(e). This part of the investigation is done using Lumerical's DEVICE SUITE FOR PHOTONIC MULTIPHYSICS SIMULATION (2020a version). The random positions of the nanospheres in the URs is decided by this software under

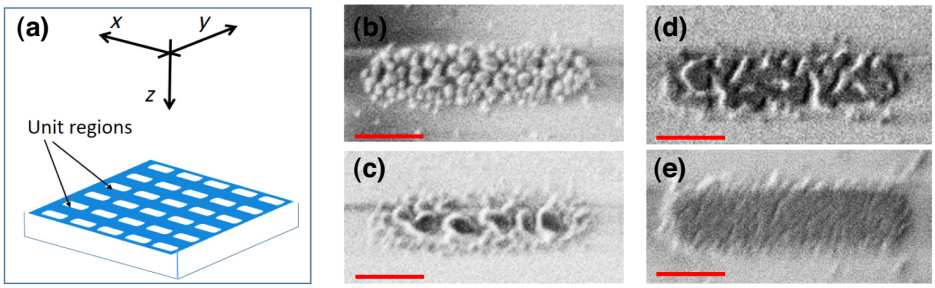

FIG. 1. (a) The template of the periodic array of unit regions (URs). (b)–(e) Top-view SEM images of the Au plasmonic architectures considered for the URs. The scale bars in these figures are 250 nm.

the condition of no overlap, i.e., isolated nanospheres, or with limited overlap. The simulation technique is also used to study the impact of variation of the number of Au of nanospheres per UR [Figs. 2(a)–2(f)]. To be consistent with the experimental results, the simulations are carried out considering $L = 800$ and $W = 200$ nm. The heights (H) of such URs, however, are varied to study the impact of close packing of the nanospheres.

III. COHERENT COUPLING OF MNPs: PHASE-CORRELATED DIPOLE DOMAINS

We start our investigation by considering the simulation results for the periodic structures as shown in Figs. 2(a)–2(f). Here, the number of nanospheres per UR (N) is considered to be 1 (a), 4 (b), 10 (c), 20 (d), 30 (e), and 38 (f). We assume the radii of such nanospheres (r) to be 30 nm and the height of the URs (H) containing such MNPs to be 50 nm. The results of the simulation, when the incident-light polarization is along the x axis (x-pol), are shown in Figs. 2(g) and 2(h). In the case of Fig. 2(g), the refractive index of the superstrate (n_{sup}) is 1 and for the case of Fig. 2(h) it is 1.5. When $N = 1$, we can see formation of a single peak at about 510 nm in (g) and 557 nm in (h). The difference can simply be associated with the increase of the refractive index of the superstrate in (h). For the case of $n_{sup} = 1$ (g), as the number of MNPs is increased, the peak is slightly red shifted. This is an indication of the rise of plasmonic inter-MNP plasmonic coupling. For the case of $n_{sup} = 1.5$ (h), however, as N increases the 560 nm peak is blue shifted, reaching 551 nm when $N = 30$. The most distinct feature seen in Fig. 2(h), however, happens at the longer-wavelength range. For the case of $N = 4$, we can see formation of a small peak at about 745 nm. As N increases to 10, this peak becomes stronger and is shifted to 751 nm. For the case of $N = 20$, we see a very sharp peak with a full width at half maximum (FWHM) of about 20 nm at 757 nm. As the number of MNPs increases further, however, this peak becomes broader and is red shifted. For the case of $N = 38$, the peak happens at 800 nm and its FWHM becomes more than 200 nm. The longer-wavelength peak seen in Fig. 2(h) does not happen when the incident light becomes polarized along the y axis (Fig. 3).

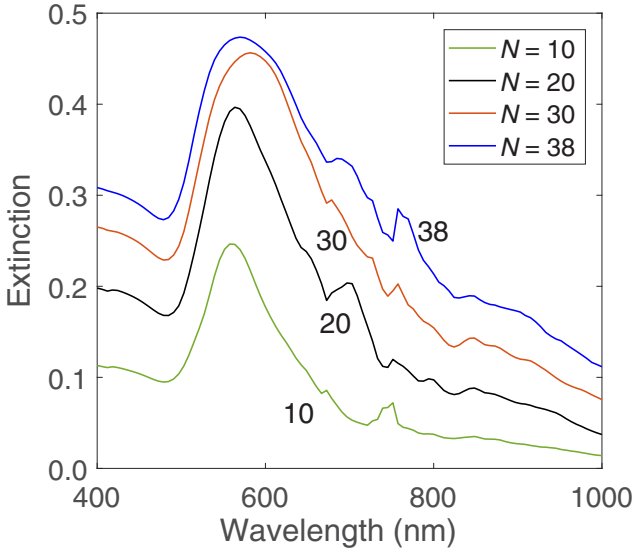

FIG. 3. The extinction spectra of the periodic structures considered in Figs. 2(c)–2(f) when the incident light is polarized along the y axis (y-pol) and n_{sup}=1.5.

To further study the impact of N, in Fig. 4 we study the modal field-enhancement factor in two adjacent URs at 557 nm (a)–(e) and 751 nm (a')–(e') for the case of Fig. 2(h). For both wavelengths, the results for $N = 1$ show the interaction of individual MNPs with the incident

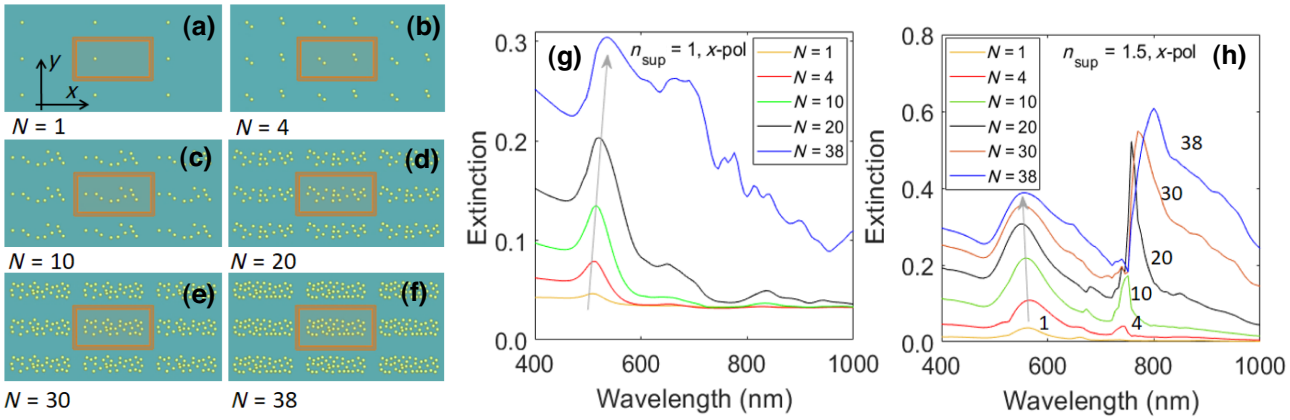

FIG. 2. (a)–(f) Periodic arrays of URs with 1, 4, 10, 20, 30, and 38 MNPs per UR, respectively. (g),(h) Simulation results for the extinction spectra associated with (a)–(f) when $n_{sup} = 1$ (g) or 1.5 (h). The incident-field polarization is considered to be along the x axis (x-pol). N in the legends refer to the number of MNPs per UR. The number close to each curve in (h) refers to its corresponding N.

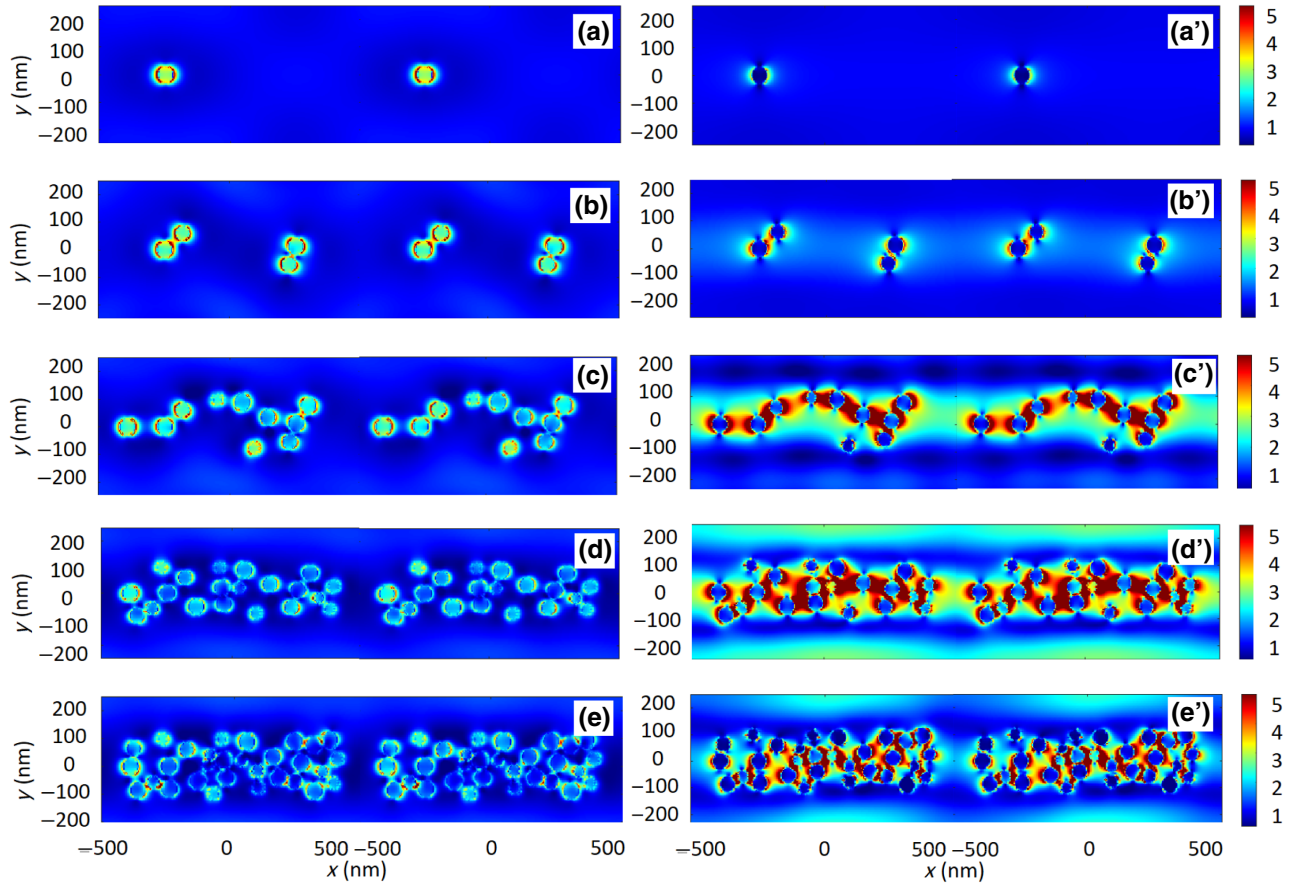

FIG. 4. The field-enhancement profiles for $N = 1$, 4, 10, 20, and 30 at (a)–(e) 557 nm and (a')–(e') 751 nm in the x-y plane, respectively. Here, $n_{sup} = 1.5$ and the incident light is polarized along the x axis (x-pol). The wavelengths here are associated with the main peaks seen Fig. 2(h).

light [Figs. 4(a) and 4(a')]. The patterns in (a) show natural dipolarlike resonance of the MNPs. In the case of (a'), however, the field pattern is different and much weaker. This can be associated with the fact that at 557 nm, the natural LSPRs of the MNPs are excited, while 751 nm is far from such resonances. For $N = 4$ at 557 nm, we can only see some inter-MNP coupling between the MNPs that are close to each other [Fig. 4(b)]. At 751 nm, however, we can see stronger near fields, with some—albeit weak—indication of optical coupling between the MNPs between the adjacent URs along the x axis [Fig. 4(b')]. For the case of $N = 10$, the situation at 557 nm does not change significantly, i.e., it shows coupling between MNPs that fall randomly close to each other [Fig. 4(c)]. At 751 nm, however, we can see a significant stimulated inter-MNP plasmonic coupling, converting each UR into a PCDD. For such a N ($N = 10$), these domains are effectively coupled to their nearest neighboring PCDDs optically along the x axis [Fig. 4(c')]. This situation is further enhanced for the case of $N = 20$, in which the PCDDs become larger as more MNPs in the URs are coherently coupled to each other [Fig. 4(d')]. For the case of $N = 30$, however, the optical coupling between the PCDDs becomes weaker, as each PCDD contains more extensive inter-MNP plasmonic coupling [Fig. 4(e')]. At 557 nm, for the cases of both $N = 20$ and $N = 30$, we mostly see inter-MNP plasmonic coupling, with much less strength than the corresponding cases at 751 nm. No inter-UR coupling or lattice modes can be seen at 557 nm.

The results shown in Fig. 2(h) suggest that for $N = 4$, 10, and 20, the peaks at approximately 751 nm are quite narrow. For $N = 30$ and 38, they become broader. Such an effect in Figs. 4(b')–4(e') can be seen as a transition from more strongly coupled PCDDs [Figs. 4(c') and 4(d')] to more localized ones [Fig. 4(e')]. This can be seen further if we inspect the mode profiles in the x-z plane that passes through the middle of the URs [Fig. 1(a)]. At 557 nm, as shown in Figs. 5(a)–5(c), no significant optical field exists. At 751 nm, in the cases of $N = 10$ and 20, however, there is a clear optical field along the x axis, connecting the neighboring PCDDs [Figs. 5(a')–5(b')]. For the case of $N = 38$, however, this field is much weaker [Fig. 5(c')]. Note that for x-pol polarization, the PCDDs are coupled together in parallel, i.e., the polarization of the incident

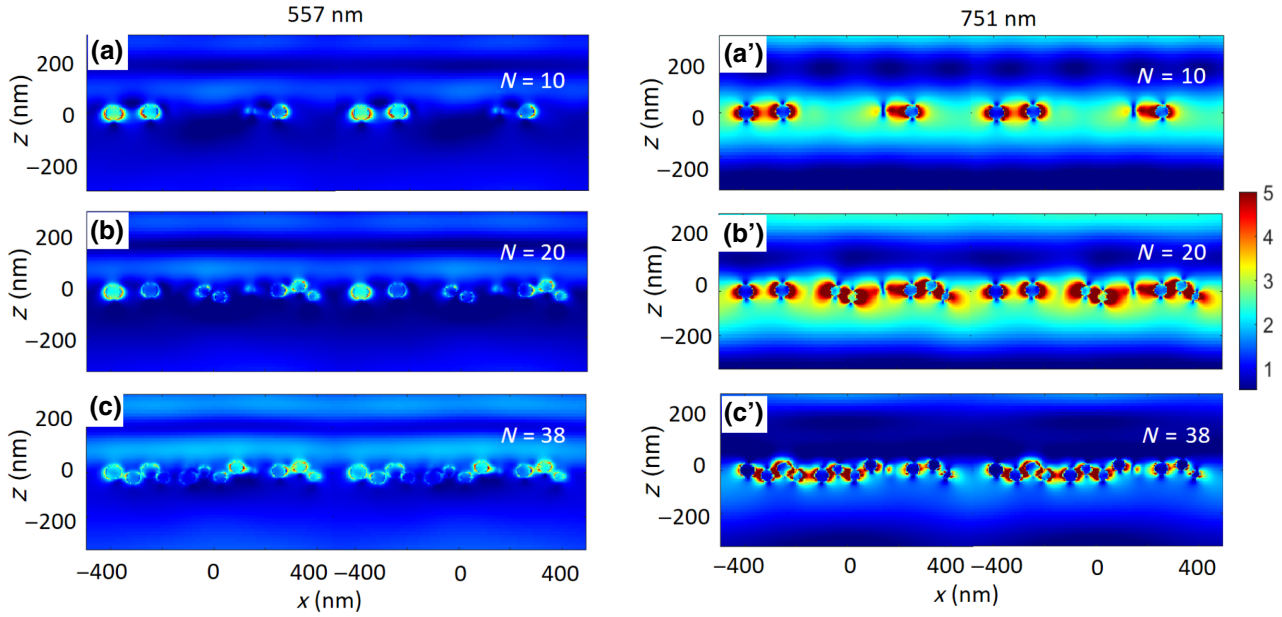

FIG. 5. The field-enhancement profiles in the x-z plane for (a),(a′) $N = 10$, (b),(b′) $N = 20$, and (c),(c′) $N = 38$ at 557 and 751 nm in two adjacent URs.

light is along the optical field coupling the PCDDs. Considering the wavelength of the RA, i.e., $\lambda_{RA} = (n/m)a$ (n is n_{sup} or n_{sub}, m is the diffraction order and a is the lattice constant), we expect, for $a = a_x$ and $n_{sub} = 1.5$, λ_{RA} to be approximately 1.47 μm for $m = 1$ and $\lambda_{RA} = 735$ nm for $m = 2$. For the case of $N = 38$, this process happens while it is convoluted by the extensive plasmonic inter-MNP coupling in each PCDD. In fact, as seen in the following, as the density of MNPs in each UR becomes larger, the optical coupling process flips from parallel coupling with $m = 2$ to orthogonal coupling with $m = 1$.

IV. LATTICE-INDUCED COUPLING OF METALLIC NANOPARTICLES WITH RANDOM SIZES

Up to now, we have considered Au nanospheres that have the same sizes. In many practical cases, MNPs have random sizes and shapes. This is particularly the case of the URs containing NISs that are experimentally studied in this paper. In this section, we start with a random distribution of nanospheres with a minimum radius (r_{min}) of 5 nm and a maximum radius (r_{max}) of 20 nm. The length (L) and width (W) of each UR containing such nanospheres are considered to be 800 and 200 nm, respectively, while their heights (H) are varied. For a given number of nanospheres per UR (N), variation of H changes the spacing between the nanospheres. In each case, however, the position of the nanospheres remains random, determined by the software used for the numerical calculations. a_x and a_y are also considered to be 1 and 0.5 μm, as in the cases considered in Fig. 2, and n_{sup} is 1.5. Figure 6(a) shows an enlarged view of the size distribution of the MNPs in a UR. We also consider that the incident light is polarized along the x axis (x-pol).

The results for the case when $H = 100$ nm are shown in Fig. 6(a') (solid line). They show a broad peak at about 555 nm and a sharp one at about 752 nm. For this case, we set the number of MNPs in each UR to be 200. If we keep $N = 200$ but reduce H to 50 nm, i.e., we reduce the volume of each UR by a half, the results are changed to some extent. As seen in this figure (dashed line), under this condition the broad peak is red shifted by about 7 nm. The narrow peak is reduced in height and becomes broader. This shows the impact of density of the MNPs, highlighting the effect of inter-MNP coupling on the hybridization of PCDDs with the RA. This can be seen further if we consider $H = 100$ but increase the number of MNPs to 600 [Fig. 6(a'), dashed-solid line]. This represents a case similar to that shown in Fig. 2(h) with $N = 38$, showing partial disentanglement of the PCDDs from the parallel diffractive modes. Note that the maximum sizes of the NISs in the case of samples 1 and 2 are about 50–100 nm. In the simulation, for better consistency of the LSPRs, we require the projected sizes of the nanospheres in the plane of the arrays to be similar to these sizes. This condition is reflected in the values of H considered in this paper.

To further study the impact of the MNP size distribution, we consider three more distinct cases. In one case, $r_{min} = 20$ and $r_{max} = 30$ nm [Fig. 6(b)]. In the second case, we consider $r_{min} = 30$ and $r_{max} = 100$ nm, depicting a much wider size distribution [Fig. 6(c)]. For the

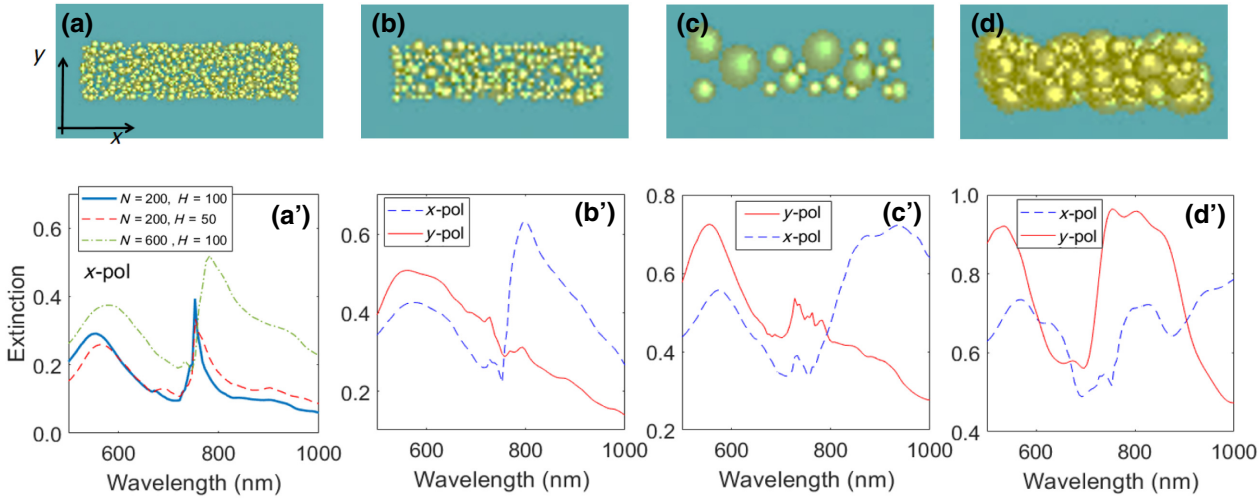

FIG. 6. Enlarged views of the URs containing an ensemble of MNPs with random sizes between (a) $r_{min} = 5$ and $r_{max} = 20$ nm, (b) $r_{min} = 20$ and $r_{max} = 30$ nm, (c) $r_{min} = 30$ and $r_{max} = 100$ nm, and (d) $r_{min} = 20$ and $r_{max} = 80$ nm with allowed overlap. (a') The extinction spectra of (a) when $N = 200$ and $H = 100$ nm (solid line), $N = 200$ and $H = 50$ nm (dashed line), and $N = 600$ and $H = 100$ nm (dashed-dotted line). (b')–(d') The simulation results for the extinction spectra of (b)–(d) for x-pol (dashed lines) and y-pol (solid lines), respectively.

third case, we consider $r_{min} = 20$ and $r_{max} = 80$ nm but also allow overlap between the MNPs [Fig. 6(d)]. The results presented in Figs. 6(b')–6(d') show the extinction spectra associated with each of these cases for x-pol and y-pol. For x-pol, the structure shown in Fig. 6(b) supports a broad peak at about 580 nm and a sharper

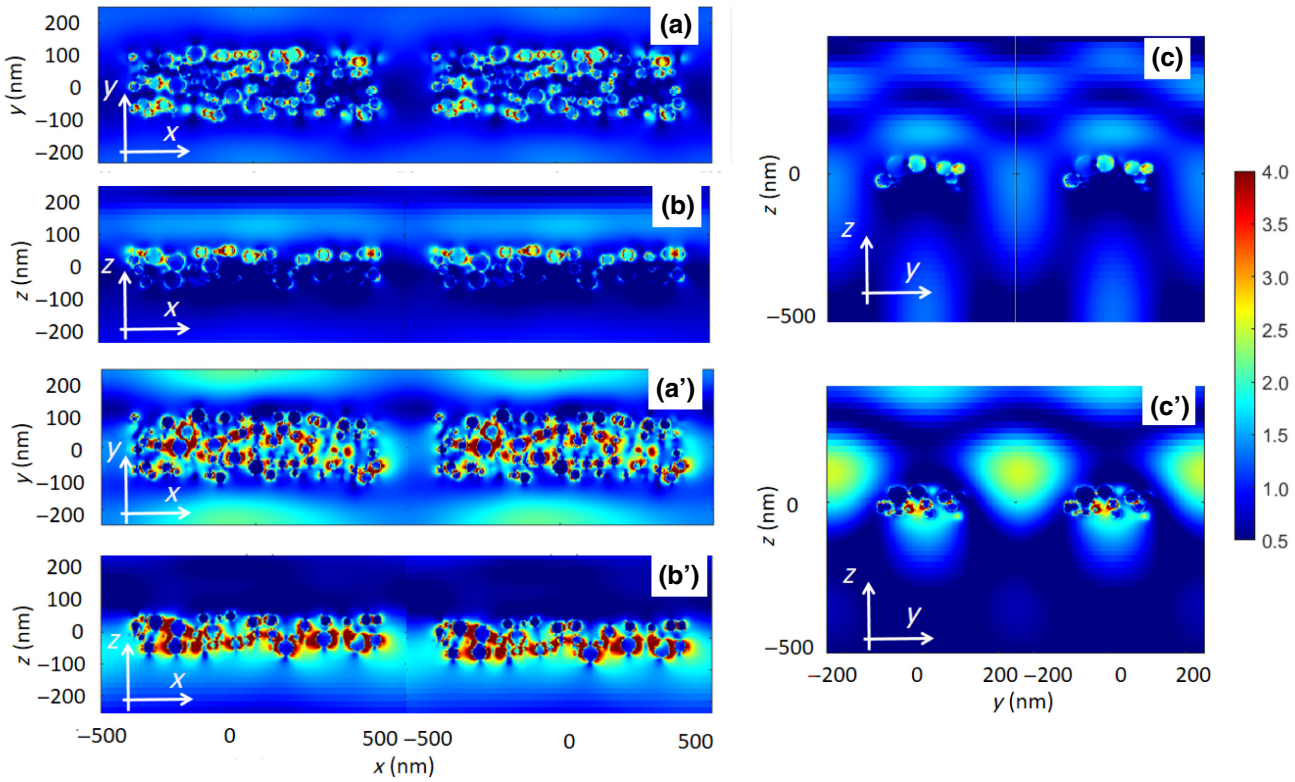

FIG. 7. The field-enhancement profiles of two adjacent URs of the periodic structure shown in Fig. 6(b) at (a)–(c) 570 nm and (a')–(c') 797 nm. Here, (a) and (a') refer to the mode in the x-y plane, (b) and (b') to the mode in the x-z plane, and (c) and (c') to the mode in the y-z plane. The incident field is considered to be polarized along the x axis (x-pol).

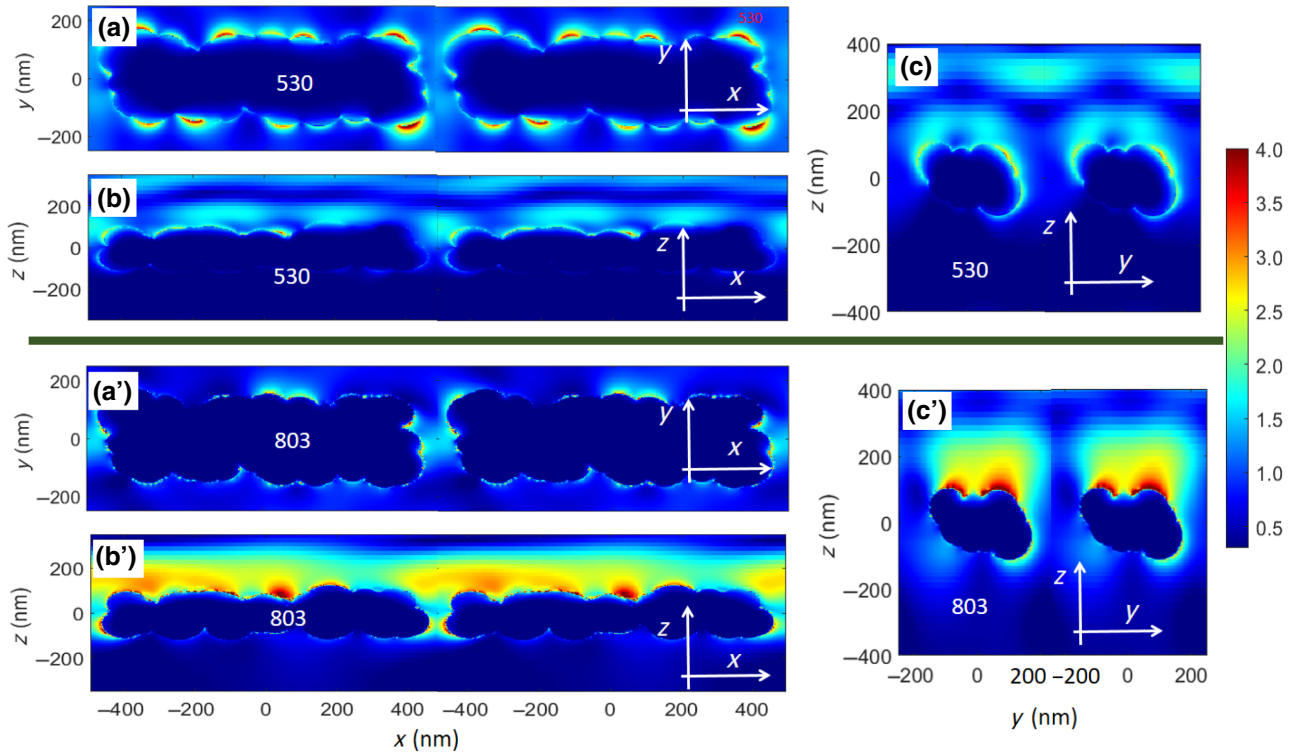

FIG. 8. The field-enhancement profiles of two adjacent URs of the periodic structure shown in Fig. 6(d) at (a)–(c) 530 and (a')–(c') 803 nm. Here, the incident field is considered to be polarized along the y axis (y-pol).

one at 800 nm (dashed line). Once the incident light becomes polarized along the y axis (y-pol), however, the peak at 800 nm mostly disappears (solid line). For the structure shown in Fig. 6(c), more or less similar features are generated [Fig. 6(c')]. Here, however, for x-pol, the shorter-wavelength peak becomes narrower, while the longer-wavelength peak becomes quite broad while undergoing some red shifting (dashed line). For the case of the structure shown in Fig. 6(d), we observe a dramatic change [Fig. 6(d')]. Here, for x-pol, no distinct peak with high amplitude is formed (dashed line). For y-pol, however, the features include a peak at 530 nm and another one at 808 nm (solid line). In other words, it seems that the features seen for the x-pol in Figs. 6(b') and 6(c') now occur for the y-pol. This suggests how the lack of isolated MNPs changes the nature of optical coupling of plasmon modes.

Figure 7 shows the field-enhancement mode profiles associated with the x-pol cases in Fig. 6(b') at 570 and

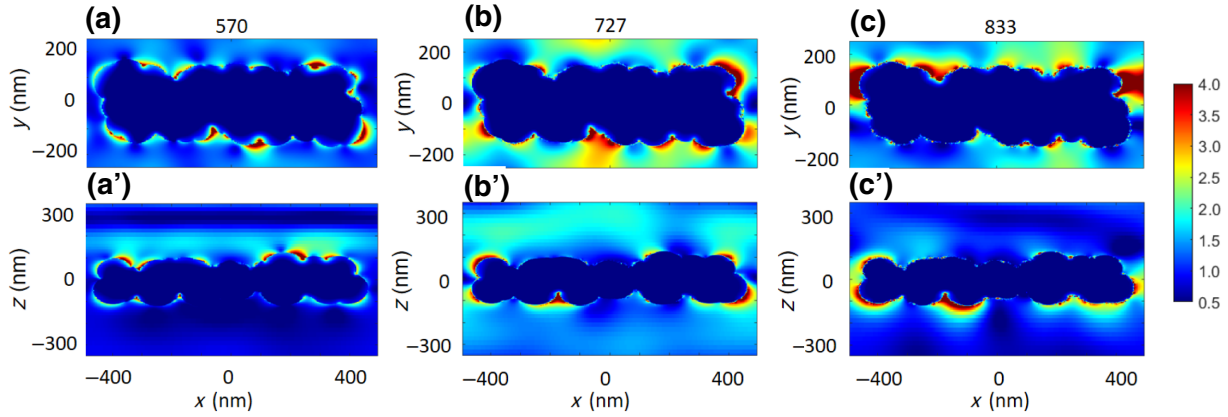

FIG. 9. The field-enhancement profiles in a UR of the periodic structure shown in Fig. 6(d) in (a)–(c) the x-y plane and (a′)–(c′) the x-z plane: (a),(a′) at 570 nm; (b),(b′) at 727 nm; (c),(c′) at 833 nm. Here, the incident field is considered to be polarized along the x axis (x-pol).

797 nm, i.e., its two main peaks. Here, we consider the modes in the x-y [(a) and (a')], x-z [(b) and (b')], y-z planes [(c) and (c')]. A clear distinction between the modes at (a)–(c) 570 nm and (a')–(c') 797 nm is the presence of the strong inter-NIS coupling in the latter, i.e., the formation of PCDDs. Figure 7(b') also shows the coupling of such domains with the neighboring ones at 797 nm via the lattice optical mode. Figure 7(c') shows a cross view of the overlap between lattice modes with the MNPs. This figure also shows the formation of field concentration regions parallel to this mode, mostly in the superstrate.

To explore the polarization-reversed optical responses of the structure in Fig. 6(d), we study its field-enhancement profiles when the incident light is polarized along the y axis (y-pol). As shown in Fig. 8, this is done for the two main wavelengths, (a)–(c) 530 nm and (a')–(c') 803 nm. The results show that the peak seen in Fig. 6(d') at 530 nm is mostly related to the edge modes of the structure. At 803 nm, however, the structure supports a much higher field enhancement [Figs. 8(a')–8(c')]. The profiles in the x-z and y-z planes in these figures show that in these cases, the field concentration and the coupling of plasmonic modes with the photonic mode mostly occurs in the superstrate [Fig. 8(b')]. These results suggest that the y-pol response seen in Fig. 6(d') is due to orthogonal coupling of the plasmon field with the first-order diffraction mode of the lattices. This highlights the formation of SLRs similar to those normally seen when the metallic nanoantennas have sufficient polarizability [34,35]. Note that for x-pol, as shown in Fig. 9, the amount of the field in the superstrate is much weaker and plasmonic coupling occurs mostly between the neighboring URs.

V. EXPERIMENTAL RESULTS

To experimentally test the results presented in the preceding section, we study the optical responses of samples 1–4 with the URs as seen in Figs. 1(b)–1(e), respectively. The array arrangement of these structures is shown in Figs. 10(a)–10(d). The case of Fig. 10(a) nearly depicts the situation considered in Fig. 6(b). The case of Fig. 10(b) offers a situation similar to that of Fig. 6(c). In these two cases, the islands are mostly separated from each other. In the case of Fig. 10(a), the NISs are small and tightly packed [Fig. 1(b)], while in the case of Fig. 10(b), they are large and well separated from each other [Fig. 1(c)]. Figure 10(c), with a UR as shown in Fig. 1(d), mimics the case shown in Fig. 6(d), in which the NISs are interconnected. The case of Fig. 10(d) offers a similar situation but the amounts of packing and interconnection of the NIS are more substantial [Fig. 1(e)].

The results of the experimental measurements are shown in Figs. 10(a')–10(d') when $n_{sup} \sim 1.33$, i.e., the superstrate is methanol. The results in Fig. 10(a') (sample 1) show that for y-pol, we see a single peak at about 600 nm. When polarization of the incident light is switched to x-pol, however, a doublet with one peak at 600 nm and the other at about 706 nm is formed. For the case of sample 2, similar features can be seen, although here the doublet is much more pronounced [Fig. 10(b')]. In fact, here the longer-wavelength peak occurs at about 780 nm. Comparison of

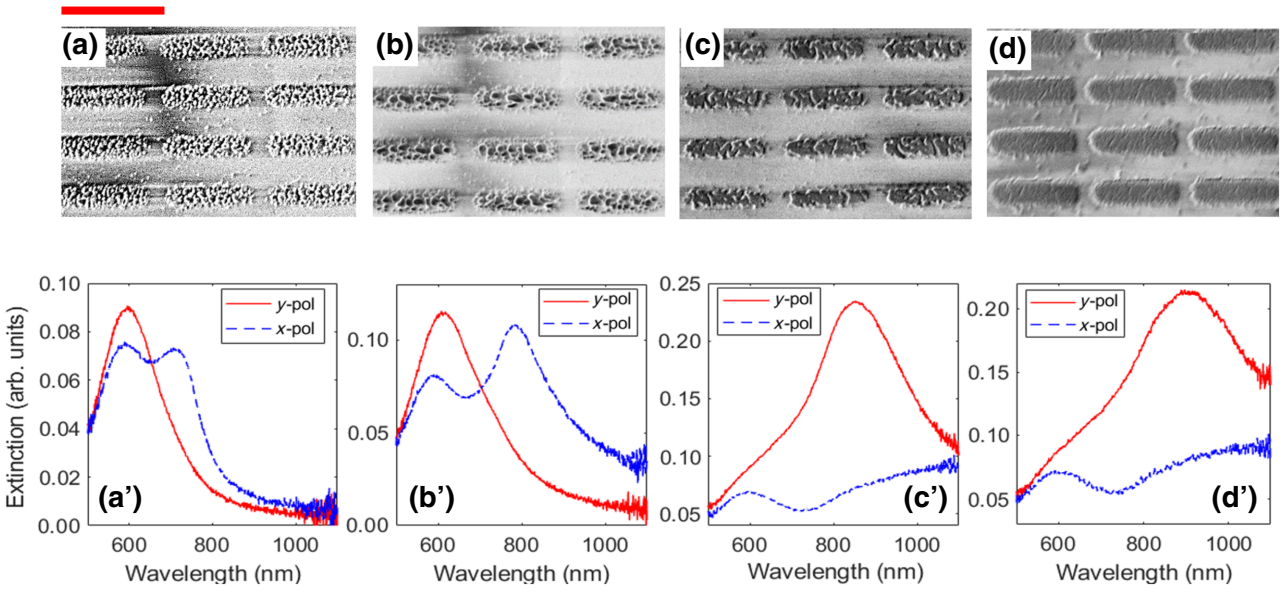

FIG. 10. (a)–(d) Top-view SEM images of the array structures with the URs shown in Figs. 1(b)–1(e), respectively. (a′)–(d′) Extinction spectra of samples 1–4 [(a)–(d)] when the incident light is polarized along the y axis (solid lines) and the x axis (dashed lines) and the refractive index of the superstrate is about 1.33. The red horizontal scale bar on the top of (a) is 1 μm.

the results for the structures shown in Figs. 4(b) and 4(c) offers a similar picture. In the case of Fig. 6(b), the second peak for x-pol occurs at about 800 nm [Fig. 6(b')]. In the structure of Fig. 6(c), which has a wider MNP size distribution, the longer-wavelength peak is broader and is red shifted [Fig. 6(c')].

For the case of sample 3, in which the NISs are large and connected to each other [Fig. 10(c)], the results in Fig. 10(c') show the polarization-reversal process. Here, for x-pol, the prominent feature includes a peak at about 600 nm. For y-pol, however, a distinct peak is formed at about 854 nm. These results are consistent with those shown for the structure in Fig. 6(d), in which we predict a reversal of the polarization response of the array [Fig. 6(d')]. A similar situation is repeated for sample 4 [Fig. 10(d)]. The surface morphology of this sample shows that the URs for this sample do not have distinct NISs [Fig. 1(e)]. The extinction spectra of this sample [Fig. 10(d')] are similar to those in Fig. 10(c'). The main difference is the width of the extinction peak, which is broader in the case of sample 4. Considering the results presented in Fig. 8, we believe that the longer-wavelength peaks in Figs. 11(c') and 11(d') are associated with SLRs caused by orthogonal hybridization of plasmonic resonances of URs with the RA.

The results for sample 1 [Fig. 10(a')] suggest that the peak at 706 nm is associated with the formation of PCDDs and inter-PCDD coupling. These can be conferred considering the results shown in Figs. 7(a')–7(c'). The nature of inter-PCDD coupling via lattice modes can be seen in the mode profiles shown in Fig. 7(b'). Figure 10(b') suggests that large NISs can act as more efficient plasmonic relays that transform a UR into a PCDD. The prime impact of this in Fig. 10(b') is the relatively sharp peak generated at 780 nm. To see this further, in Fig. 11 we show the field-enhancement profile in the (a1) x-y and (a2) x-z planes at 909 nm for the structure shown in Fig. 6(c). At this wavelength, as shown in Fig. 6(c'), the extinction spectrum supports a strong peak for x-pol. Figure 11 shows the considerable role that MNPs play as efficient interconnecting plasmonic antennas for effective formation of PCDDs.

Note that the optical responses of samples 1 and 2 for y-pol are very similar to those of NISs without any periodicity. To see this, in Figs. 11(b) and 11(c) we present surface morphologies of the reference samples that are similar to those of the URs of sample 2 [Fig. 10(b)] and sample 4 [Fig. 10(d)], but without any array structure. Figure 11(d) shows the extinction spectra of these samples. For the case of Fig. 11(b), we see a peak at about 567 nm, very similar to that seen for the y-pol of sample 2

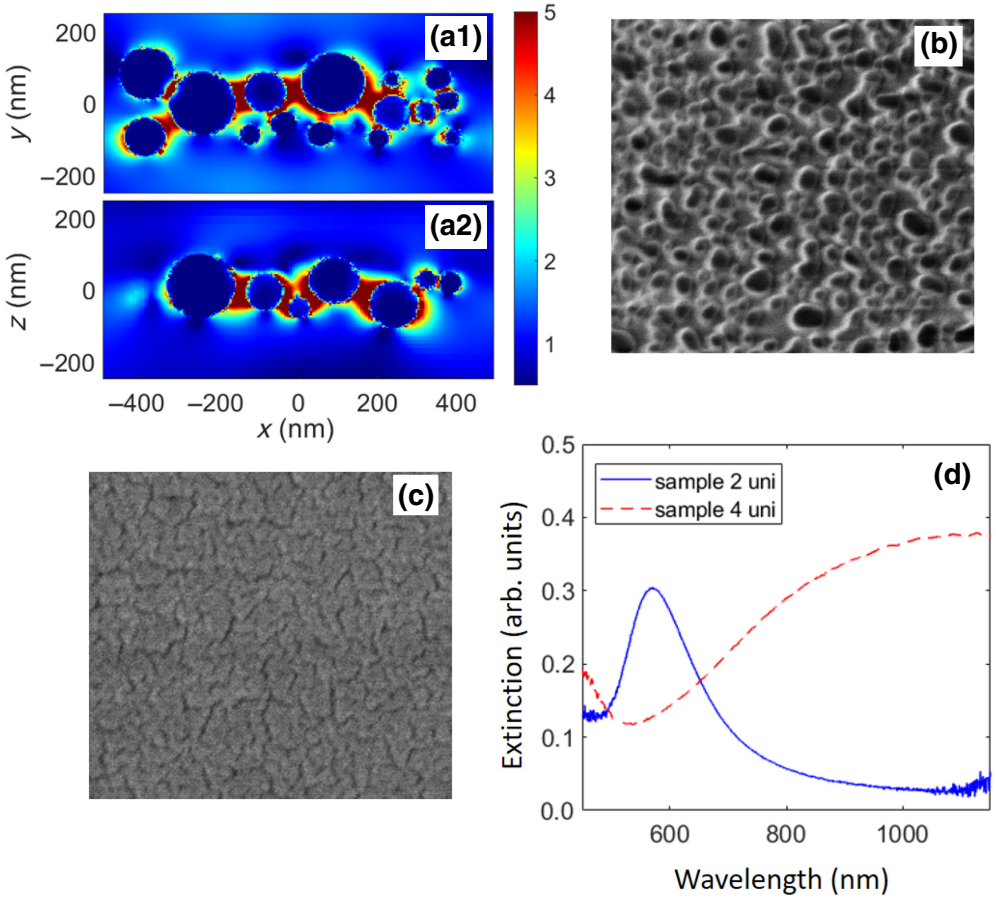

FIG. 11. (a1),(a2) The results of simulations for the case of the structure shown in Fig. 6(c) in the x-y and x-z planes, respectively. (b),(c) SEM images of the structures that support the same surface morphology as those in samples 2 and 4 but without any periodicity. The solid and dashed lines in (d) show the extinction spectra associated with (b) and (c), respectively.

(Fig. 10(b'), solid line). For the case of the structure shown in Fig. 11(c), however, we mostly see a continuous rise toward the infrared range (dashed line). This feature matches well with the results seen in Figs. 7(c') and 7(d') for x-pol.

VI. CONCLUSIONS

We study the optics of periodic arrays of metallic nanostructure units with distinct plasmonic architectures. These units support different regimes of plasmonic coherent coupling of NISs. We use such structures to study the formation of phase-correlated dipole domains, in which coherent intra-UR coupling between MNPs forms collective resonances. We demonstrate how such coupling is driven by the lattice-enhanced plasmonic modes of the MNPs at frequencies that are quite different from the intrinsic LSPRs of the MNPs. We study the coherent coupling of PCDDs and the formation of collective states associated with SLRs. The results show the optimized structure for PCDDs and efficient inter-PCDDs. The experimental results confirm the key predictions of the numerical results.

ACKNOWLEDGMENTS

This work is supported by the U.S. National Science Foundation under Grant No. ECCS-1917544.

[1] M. Quinten, A. Leitner, J. R. Krenn, and F. R. Aussenegg, Electromagnetic energy transport via linear chains of silver nanoparticles, Opt. Lett. **23**, 1331 (1998).

[2] S. A. Maier, P. G. Kik, H. A. Atwater, S. Meltzer, E. Harel, B. E. Koel, and A. A. G. Requicha, Local detection of electromagnetic energy transport below the diffraction limit in metal nanoparticle plasmon waveguides, Nat. Mater. **2**, 229 (2003).

[3] S. A. Maier, P. G. Kik, and H. A. Atwater, Observation of coupled plasmon-polariton modes in Au nanoparticle chain waveguides of different lengths: Estimation of waveguide loss, Appl. Phys. Lett. **81**, 1714 (2002).

[4] M. L. Brongersma, J. W. Hartman, and H. A. Atwater, Electromagnetic energy transfer and switching in nanoparticle chain arrays below the diffraction limit, Phys. Rev. B **62**, R16356 (2000).

[5] N. J. Halas, S. Lal, W.-S. Chang, S. Link, and P. Nordlander, Plasmons in strongly coupled metallic nanostructures, Chem. Rev. **111**, 3913 (2011).

[6] D. Solis Jr, B. Willingham, S. L. Nauert, L. S. Slaughter, J. Olson, P. Swanglap, A. Paul, W.-S. Chang, and S. Link, Electromagnetic energy transport in nanoparticle chains via dark plasmon modes, Nano Lett. **12**, 1349 (2012).

[7] B. Willingham and S. Link, Energy transport in metal nanoparticle chains via sub-radiant plasmon modes, Opt. Express **19**, 6450 (2011).

[8] S. A. Maier, M. L. Brongersma, P. G. Kik, S Meltzer, A. A. G. Requicha, B. E. Koel, and H. A. Atwater, Plasmonics—A route to nanoscale optical devices (vol. 13, pp. 1501, 2001), Adv. Mater. **15**, 562 (2003).

[9] X. Han, Y. Liu, and Y. Yin, Colorimetric stress memory sensor based on disassembly of gold nanoparticle chains, Nano Lett. **14**, 2466 (2014).

[10] A. Apuzzo, M. Février, R. Salas-Montiel, A. Bruyant, A. Chelnokov, G. Lérondel, B. Dagens, and S. Blaize, Observation of near-field dipolar interactions involved in a metal nanoparticle chain waveguide, Nano Lett. **13**, 1000 (2013).

[11] S. R. Pocock, X. Xiao, P. A. Huidobro, and V. Giannini, Topological plasmonic chain with retardation and radiative effects, ACS Photonics **5**, 2271 (2018).

[12] J. J. De Jonge, M. A. Ratner, S. W. De Leeuw, and R. O. Simonis, Controlling the energy transfer in dipole chains, J. Phys. Chem. B **110**, 442 (2006).

[13] S. M. Sadeghi, R. R. Gutha, and C. Sharp, Coherent optical coupling of plasmonic dipoles in metallic nanoislands with random sizes and shapes, J. Mater. Chem. C **7**, 9678 (2019).

[14] S. R. K. Rodriguez and J. Gómez Rivas, Surface lattice resonances strongly coupled to Rhodamine 6G excitons: Tuning the plasmon-exciton-polariton mass and composition, Opt. Express **21**, 27411 (2013).

[15] L. Shi, T. K. Hakala, H. T. Rekola, J-P. Martikainen, R. J. Moerland, and P. Törmä, Spatial Coherence Properties of Organic Molecules Coupled to Plasmonic Surface Lattice Resonances in the Weak and Strong Coupling Regimes, Phys. Rev. Lett. **112**, 153002 (2014).

[16] W. Liu, B. Lee, C. H. Naylor, H.-S. Ee, J. Park, A. T. C. Johnson, and R. Agarwal, Strong exciton-plasmon coupling in MoS_2 coupled with plasmonic lattice, Nano Lett. **16**, 1262 (2016).

[17] R. R. Gutha, S. M. Sadeghi, C. Sharp, and W. J. Wing, Biological sensing using hybridization phase of plasmonic resonances with photonic lattice modes in arrays of gold nanoantennas, Nanotechnology **28**, 355504 (2017).

[18] X. Zhang, S. Feng, J. Zhang, T. Zhai, H. Liu, and Z. Pang, Sensors based on plasmonic-photonic coupling in metallic photonic crystals, Sensors **12**, 12082 (2012).

[19] B. D. Thackray, V. G. Kravets, F. Schedin, G. Auton, P. A. Thomas, and A. N. Grigorenko, Narrow collective plasmon resonances in nanostructure arrays observed at normal light incidence for simplified sensing in asymmetric air and water environments, ACS Photonics **1**, 1116 (2014).

[20] B. Auguié and W. L. Barnes, Collective Resonances in Gold Nanoparticle Arrays, Phys. Rev. Lett. **101**, 143902 (2008).

[21] Y. Sonnefraud, N. Verellen, H. Sobhani, G. A. E. Vandenbosch, V. V. Moshchalkov, P. Van Dorpe, P. Nordlander, and S. A. Maier, Experimental realization of subradiant, superradiant, and Fano resonances in ring/disk plasmonic nanocavities, ACS Nano **4**, 1664 (2010).

[22] E. M. Hicks, X. Zhang, S. Zou, O. Lyandres, K. G. Spears, G. C. Schatz, and R. P. Van Duyne, Plasmonic properties of film over nanowell surfaces fabricated by nanosphere lithography, J. Phys. Chem. B **109**, 22351 (2005).

[23] J. Li, J. Ye, C. Chen, L. Hermans, N. Verellen, J. Ryken, H. Jans, W. Van Roy, V. V. Moshchalkov, and L. Lagae *et al.*, Biosensing using diffractively coupled plasmonic crystals: The figure of merit revisited, Adv. Opt. Mater. **3**, 176 (2015).

[24] S. M. Sadeghi, W. J. Wing, and Q. Campbell, Tunable plasmonic-lattice mode sensors with ultrahigh sensitivities and figure-of-merits, J. Appl. Phys. **119**, 244503 (2016).

[25] S. M. Sadeghi, R. R. Gutha, and W. J. Wing, Turning on plasmonic lattice modes in metallic nanoantenna arrays via silicon thin films, Opt. Lett. **41**, 3367 (2016).

[26] R. Guo, S. Derom, A. I. Väkeväinen, R. J. A van Dijk-Moes, P. Liljeroth, D. Vanmaekelbergh, and P. Törmä, Controlling quantum dot emission by plasmonic nanoarrays, Opt. Express **23**, 28206 (2015).

[27] M. Ramezani, G. Lozano, M. A. Verschuuren, and J. Gómez-Rivas, Modified emission of extended light emitting layers by selective coupling to collective lattice resonances, Phys. Rev. B **94**, 125406 (2016).

[28] X. W. Yuan, L. Shi, Qi Wang, C. Q. Chen, X. H. Liu, L. X. Sun, B. O. Zhang, J. Zi, and W. Lu, Spontaneous emission modulation of colloidal quantum dots via efficient coupling with hybrid plasmonic photonic crystal, Opt. Express **22**, 23473 (2014).

[29] R. R. Gutha, S. M. Sadeghi, C. Sharp, A. Hatef, and Y. Lin, Multi-order surface lattice resonances and dark mode activation in metallic nanoantenna arrays, J. Appl. Phys. **125**, 023103 (2019).

[30] N. Liu, M. Mesch, T. Weiss, M. Hentschel, and H. Giessen, Infrared perfect absorber and its application as plasmonic sensor, Nano Lett. **10**, 2342 (2010).

[31] R. J. Bettles, S. A. Gardiner, and C. S. Adams, Enhanced Optical Cross Section via Collective Coupling of Atomic Dipoles in a 2D Array, Phys. Rev. Lett. **116**, 103602 (2016).

[32] F. Fassioli, R. Dinshaw, P. C. Arpin, and G. D. Scholes, Photosynthetic light harvesting: Excitons and coherence, J. R. Soc. Interface **11**, 20130901 (2014).

[33] J. Perczel, J. Borregaard, D. E. Chang, H. Pichler, S. F. Yelin, P. Zoller, and M. D. Lukin, Photonic band structure of two-dimensional atomic lattices, Phys. Rev. A **96**, 063801 (2017).

[34] S. M. Sadeghi, R. R. Gutha, C. Sharp, and A. Hatef, Mapping lattice-induced plasmon modes in metallic nanoantenna arrays using fluorescence decay of semiconductor quantum dot bioconjugates, Opt. Mater. **85**, 356 (2018).

[35] S. R. K. Rodriguez, A. Abass, B. Maes, O. T. A. Janssen, G. Vecchi, and J. Gómez Rivas, Coupling Bright and Dark Plasmonic Lattice Resonances, Phys. Rev. X **1**, 021019 (2011).